ELSEVIER

Catalysis Today 67 (2001) 341–355

CATALYSIS TODAY

www.elsevier.com/locate/cattod

Combinatorial discovery of bifunctional oxygen reduction — water oxidation electrocatalysts for regenerative fuel cells

Guoying Chen [a], David A. Delafuente [a], S. Sarangapani [b], Thomas E. Mallouk [a,*]

[a] *Department of Chemistry, The Pennsylvania State University, University Park, PA 16802, USA*
[b] *ICET Inc., 916 Pleasant St., Unit 12, Norwood, MA 02062, USA*

Abstract

Electrode arrays containing 715 unique combinations of five elements (Pt, Ru, Os, Ir, and Rh) were prepared by borohydride reaction of aqueous metal salts, and were screened for activity as oxygen reduction and water oxidation catalysts. Using a consensus map, catalysts that showed high activity for both reactions and good resistance to anodic corrosion were identified in the Pt–Ru rich region of the Pt–Ru–Ir ternary. The ternary catalyst $Pt_{4.5}Ru_4Ir_{0.5}$ (subscripts indicate atomic ratios) is significantly more active than the previously described Pt_1Ir_1 bifunctional catalyst for both reactions. While the best ternary catalyst is close to Pt_1Ru_1 in composition, the latter is unstable with respect to anodic corrosion. A detailed kinetic comparison of anodically stable catalysts $Pt_{4.5}Ru_4Ir_{0.5}$ and Pt_1Ir_1 showed that the addition of the oxophilic element Ru increases the reaction rate by stabilizing S–O bonds (S ≡ surface atom) and accelerating the oxidative deprotonation of S–OH groups.

Keywords: Fuel cell; Regenerative fuel cell; Electrocatalyst; Bifunctional catalyst; Combinatorial; Water oxidation; Oxygen reduction; Optical screening; Consensus map

1. Introduction

Combinatorial chemistry, while most popularly used in the discovery of biochemicals and pharmaceuticals, has also for many years been used to identify and optimize inorganic materials of complex compositions [1,2]. The combinatorial method entails the synthesis of large libraries of compounds, in which composition or processing conditions are systematically varied, followed by screening for a particular property of interest. Recently, this approach has been used with some success in the discovery of new catalysts [3–6], and sophisticated methods for rapid screening of catalyst libraries have now been developed [7–10].

The combinatorial approach differs from other systematic experimental methods [11–15] in one particularly important respect: combinatorial analysis relies on parallel or rapid serial testing of many catalyst samples, in such a way that the figure of merit (reaction rate, selectivity, stability, etc.) is determined without bias for all members of the library. More efficient optimization methods do the testing in a serial or serial–parallel manner and use the information from earlier experiments to determine where to look next. For example, in simplex optimization of catalysts, the next composition to be formulated and tested is determined by the relative merit of the data point obtained in the previous cycle. While systematic methods are particularly efficient for evaluating catalyst compositions — particularly when testing is the most

* Corresponding author. Tel.: +1-814-863-9637; fax: +1-814-863-8403.
E-mail address: tom@chem.psu.edu (T.E. Mallouk).

0920-5861/01/$ – see front matter
PII: S0920-5861(01)00327-3

time-consuming step in the process — they are put at a serious disadvantage when two or more variables (such as activity and selectivity) must be optimized simultaneously. This is because these variables will rarely optimize to the same composition. However, the combinatorial method, which provides data on all members of a large catalyst library, can be used to find consensus regions of parameter space that reasonably optimize all the variables of interest. In this paper, we describe the combinatorial discovery of *bifunctional* electrocatalysts. These catalysts are simultaneously optimized, using consensus maps, for activity in the reduction of oxygen to water and for the reverse reaction, the oxidation of water to oxygen. In addition, we restrict the search to catalysts that are stable in the latter anodic process in acidic electrolytes.

Bifunctional electrocatalysts are of particular interest for use in regenerative fuel cells. The possible applications of these fuel cells include unmanned platforms in low-earth orbit (LEO) and in geosynchronous-earth orbit (GEO) [16]. The permanently manned LEO space station and orbital transfer vehicles between LEO and GEO require them to be self-sufficient. They should have the versatility to convert solar energy during the sunlit portion of the orbit into fuel and to generate power during the dark portion by means of the same systems. Similar considerations apply to fuel cells for other long-term space applications, such those intended for use on planetary missions. There are also terrestrial applications for regenerative fuel cells that include back-up power, electrical load-leveling, stand-alone photovoltaic power systems [17–20], and remote or portable power plants [21,22]. In all these applications, the combined requirements for economy of space, weight, materials, and design simplicity lead to devices in which an electrolyzer and a fuel cell work in tandem as an electrical energy storage and generation system.

A regenerative fuel cell is a battery-like hydrogen/oxygen system, which offers the possibility of splitting water by electrolysis, storing the hydrogen gas (and in some applications the oxygen gas as well) and then generating electricity by the fuel cell process. It has the distinct advantage over state-of-the-art battery systems in that power and energy are separated, since the energy is directly related to the fuel storage, while the rated power depends on the electrode area. This means that simply increasing reactant storage, without changing the reactor stack(s) can increase the stored energy. The result is that the mass advantage of typical advanced batteries loses out to that of regenerative fuel cells when the discharge time is increased beyond a few tens of minutes.

Despite their apparent advantages, regenerative fuel cells are still in their early stages of development because of two limiting factors: system efficiency and cost. An important step towards the reduction of cost is the concept of using only one converter for the electrolyzer and the fuel cell. In these systems, one electrode is used solely for the oxygen reactions (oxygen evolution in the electrolysis mode, oxygen reduction in the fuel cell mode), whereas the other operates as the corresponding hydrogen electrode (hydrogen evolution in the electrolysis mode, hydrogen oxidation in the fuel cell mode). With favorable kinetics of hydrogen electrocatalysis on platinum, improvement of the kinetics of oxygen electrocatalysis for both reactions — oxygen reduction and water oxidation — is crucial. Previous studies have found that at the oxygen electrode in regenerative fuel cells, the preferred oxygen reduction catalysts have poor oxygen evolution performance, and the preferred oxygen evolution catalysts have poor fuel cell performance. Moreover, catalysts at the oxygen electrodes tend to corrode at the very positive potentials used in the electrolysis mode. This effect decreases the performance of the catalyst quickly, and so the lifetime of the catalyst is not adequate for most applications. Thus, there is a need to discover new electrocatalytic materials that can resist corrosion and also catalyze both the oxygen reduction and oxygen evolution reactions efficiently.

The first attempt to develop oxygen electrocatalysts was made using nickel and nickel oxide catalysts in the form of ‘valve-electrodes’ [23]. Since then, many studies pertaining to oxygen electrocatalysis in regenerative fuel cells have been published. The catalytic materials used are in general metal alloys and oxides. A corrosion study of several mixed oxides in alkaline electrolyte solutions has been identified sodium–platinum oxide and lead–iridium oxide compositions as promising catalysts [24]. More recent studies have shown that Pt_{50}/Ir_{50} (numbers in subscripts indicate atomic ratios) or 50% Pt/50% IrO_2 (wt.%) can be used in regenerative fuel cells. Reasonable efficiencies and lifetimes were achieved [25–27]. Other studies have shown that Rh/Ru (1:1)-oxide and

Ir/Rh (1:2)-oxide are also promising oxygen electrode catalysts in regenerative fuel cells.

2. Experimental

2.1. Synthesis of combinatorial arrays

Electrode arrays were prepared by dispersing aqueous solutions of five metal salts ($RhCl_3$, H_2PtCl_6, $RuCl_3$, $OsCl_3$ and $IrBr_3$) onto a Teflon-coated Toray carbon sheet, using a robotic plotter (Cartesian Technologies, PixSys 3200). The completed array contained the same total number of moles of metal at each spot. A 40-fold molar excess of 5% aqueous sodium borohydride was added to each spot, and the reduced array was thoroughly washed with nanopure water (18.3 MΩ/cm).

2.2. Screening of catalysts for anode (water oxidation) and cathode (oxygen reduction) reactions

The screening process was carried out in a three-electrode gas diffusion cell, with the catalyst-containing array as the working electrode, Pt gauze as the counter electrode and RHE (reversible hydrogen electrode) as the reference. An indicator solution containing Ni–PTP (pH = 3) was used as the electrolyte for oxygen evolution [28]. After the array was conditioned at +1600 mV (vs. RHE) for 30 min (during which most of the catalyst spots lost their activity due to corrosion), the potential was increased in 50 mV steps, starting at +1200 mV (vs. RHE), until visible fluorescence was observed. The array was then washed thoroughly with deionized water and assembled again as the working electrode of the three-electrode cell for oxygen reduction screening. An indicator solution containing Phloxine B (pH = 2.7) was used as the electrolyte. After the array was conditioned at +600 mV (vs. RHE) for 30 min, the potential was decreased in 50 mV steps from +900 mV (vs. RHE) until visible fluorescence was observed.

2.3. Preparation of unsupported high surface area catalysts

High surface area catalysts were prepared by mixing appropriate amounts of metal chloride salts in deionized water to an overall concentration of 10 mM. A 5% solution of aqueous sodium borohydride was added portionwise until a 40-fold molar excess was achieved. The precipitate was washed repeatedly with deionized water and dried at 80°C. The filtrates were analyzed by ICP-AES, and the results showed that the reduction of metal ions under the conditions used was essentially quantitative.

2.4. X-ray photoelectron spectroscopy (XPS) and X-ray diffraction

XPS were obtained with a Kratos Analytical XSAM 800 PCI spectrometer, which had a Mg Kα line source. Powder samples were dusted onto double-sided carbon tape, with a spot size of 700 μm (iris open) and a take-off angle of 80° (with respect to the sample plane). The approximate sampling depth under these conditions was 25 Å. Binding energies were referenced to a graphite standard (C 1s = 284.6 eV), and apparent atomic percentages were obtained by dividing integrated peak areas by relative sensitivity factors (RSFs).

X-ray powder diffraction patterns were recorded on a Philips X'Pert MPD diffractometer, using monochromatized Cu Kα radiation (λ = 1.5418 Å).

2.5. Scanning electron microscopy (SEM) and UV–visible spectra

SEM images were obtained at the electron microscope facility at the Pennsylvania State University, using a JEOL-JSM 5400 microscope at 30 kV accelerating voltage. UV–visible spectra of solutions were obtained on a Hewlett Packard 8452A diode array spectrophotometer.

2.6. Surface area measurements

Surface area measurements were performed on a Micrometitics ASAP 2010 instrument. All the samples were dried under vacuum at 60°C for 15 h prior to analysis. Standard isotherms were obtained using liquid N_2 at 77 K, and a multipoint Brunauer–Emmet–Teller (BET) analysis with adsorption data in the range $0.08 < p/p_0 < 0.15$ was used for surface area calculations.

Electrochemically active surface areas were estimated based on coulometric analysis of hydrogen (H) desorption waves in the corresponding cyclic voltammetric studies. Catalyst inks for rotating disk electrode (RDE) studies were prepared by the method of TamizhMani et al. [29]. A 10 μl volume of ink was pipetted onto the surface of a glassy carbon rod (Alfa AESAR, 7 mm diameter), which was polished (1 μm diamond paste) and ultrasonically cleaned in deionized water for 10 min. The electrodes were then dried at 80°C for 10 min. Voltammetric studies were carried out under Ar using an EG&G PARC Model 363 potentiostat/galvanostat. All potentials are reported vs. RHE. The working electrodes were rotated at 2000 rpm, and cycled between 0 and 0.6 V (10 mV/s) in 0.5 M H_2SO_4, after purging with argon for 1 h. The H desorption integrals were obtained from the fifth scan. The active surface area of the catalysts was estimated by assuming 210 mC/cm^2 for the adsorption of a monolayer of H_2 on the catalyst surface [30].

2.7. Preparation and testing of half-cell electrodes

Catalyst inks for testing in gas diffusion electrodes were prepared by the method of Wilson and Gottesfeld [31], and were applied to Teflon-coated Toray carbon discs by means of a paintbrush (metal loadings were 0.8–0.9 mg/cm^2). The electrodes were then heated under Ar at 120°C for 1 h.

The painted electrode discs were then assembled as the working electrode of a three-electrode cell with Pt gauze as the counter electrode and RHE as the reference electrode. A 0.5 M H_2SO_4 solution was used as the electrolyte. For oxygen evolution experiments, Ar was used to purge the solution and current was measured as a function of applied potential (from +1200 to +1800 mV vs. RHE), after 30 min of conditioning at +1600 mV. For oxygen reduction experiments, oxygen was introduced from the back of the Teflon-coated Toray carbon working electrode, using a piece of carbon cloth to diffuse the gas flow, at a pressure of 1 in. of water (equal to the height of the electrolyte in the cell). Current–voltage curves (from +1000 to +300 mV vs. RHE) were recorded after 30 min of conditioning at 600 mV. All electrode areas were approximately 2.45 cm^2.

2.8. pH dependent and temperature dependent voltammetry

Various solutions with different activities of H^+ ions were prepared by mixing 0.5 M H_2SO_4 with 0.5 M K_2SO_4. Polarization measurements for both anode and cathode reactions were carried out potentiostatically in these solutions in a gas diffusion cell. The anodic and cathodic polarization curves were measured at solution temperatures between 27 and 50°C, which were controlled to an accuracy of ±0.1°C.

3. Results and discussion

3.1. Mapping and fabrication of electrode arrays

Combinations of several different elements can be tested systematically as catalysts by mapping the composition space in the manner of a phase diagram. We prepared combinations of five different elements (Pt, Ru, Rh, Ir, and Os) by mapping the four-dimensional composition space into a planar array of discrete spots. At the resolution of 10 spots along each binary edge, this full pentanary map contains 715 unique combinations. The mapping and fabrication strategies have been described in detail elsewhere [28,32]. The arrays were plotted on Toray carbon sheets, in such a way that each 2 mm diameter catalyst spot contained the same number of moles of metal, at a loading of approximately 1 mg/cm^2.

3.2. Fluorescent detection of electrocatalytic activity

All electrochemical half-cell reactions, as a consequence of the condition of local electroneutrality, either generate or consume ions. In the case of water oxidation and oxygen reduction, reactions (1) and (2), H^+ ions are generated and consumed, respectively.

$$2H_2O\,(l) = O_2\,(g) + 4H^+ + 4e^- \quad (1)$$

$$O_2\,(g) + 4H^+ + 4e^- = 2H_2O\,(l) \quad (2)$$

In the electrode arrays used in this work, all the catalyst spots are short-circuited together (i.e., held at the same potential) by the conductive carbon backing material. The most active catalyst compositions produce the greatest local pH change at the lowest overpotential. Compositions that catalyze the oxygen evolution

reaction at a given applied potential generate a more acidic pH in the area immediately surrounding the electrode spot than less active compositions. Similarly, compositions that catalyze the oxygen reduction reaction create a more alkaline pH in the area immediately surrounding the electrode spot than less active catalysts. In quiescent, unbuffered solutions, these differences can be as much as 3–4 pH units. By using an indicator that is fluorescent in the appropriate form (acid or conjugate base), one can determine

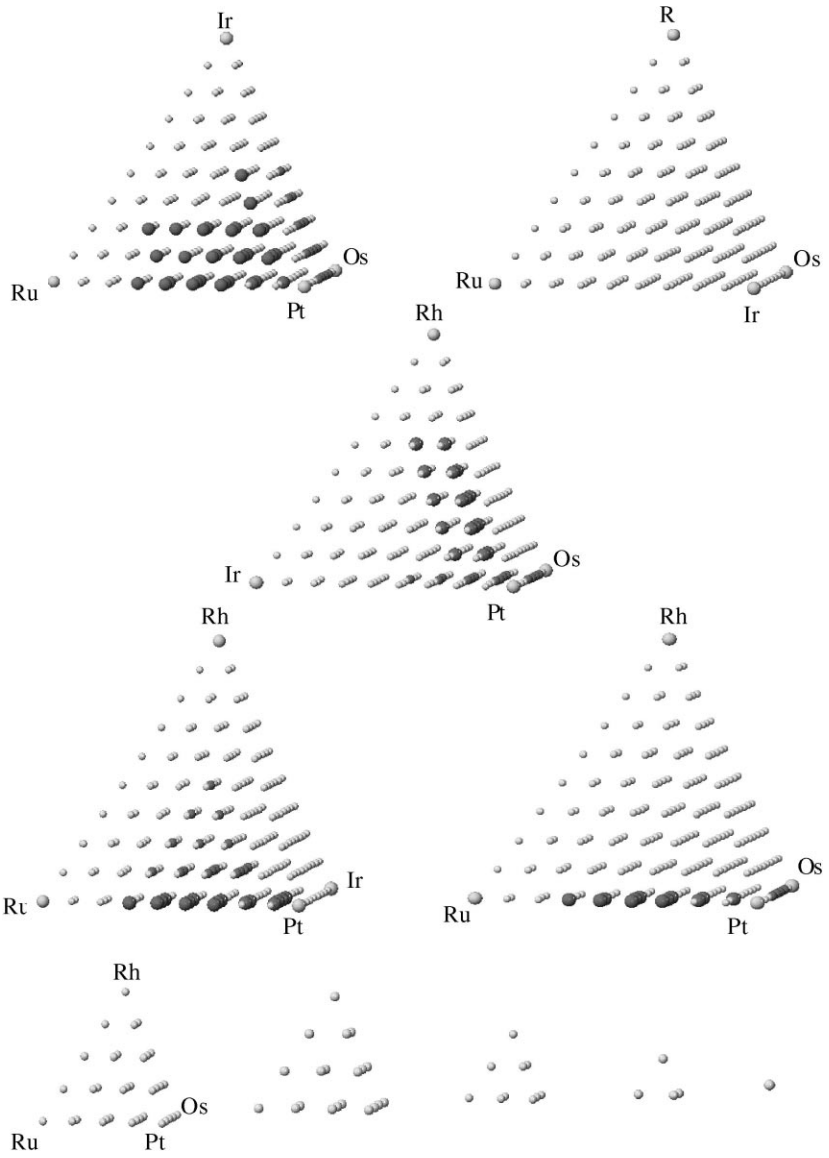

Fig. 1. Catalyst activity map for oxygen reduction. Large tetrahedra represent quaternary regions of the map, with ternary faces, binary edges, and elemental vertices. The five smaller tetrahedra at the bottom of the figure are tetrahedral sections of the pentanary region of the composition map, with Ir content increasing progressively from left to right, from 11 to 55%. Larger gray spheres indicate compositions that gave visible fluorescence from Phloxine B at +550 mV, and smaller gray spheres indicate those that were slightly less active (fluorescence at +500 mV).

optically which areas of composition space are the most active for a particular anode or cathode reaction [28]. Fluorescent pH indicators (Ni^{2+} complexed with 3-pyridine-2-yl-⟨4,5,6⟩triazolo-⟨1,5-a⟩pyridine (Ni–PTP) and Phloxine B) [32] were used for anode and cathode reactions (1) and (2), respectively, in these optical screening experiments.

3.3. Catalyst screening results

The results of the optical screening experiments can be expressed in three-dimensional tetrahedral sections of a four-dimensional pentanary activity map, as shown in Figs. 1–3. The spheres in each diagram correspond to a particular composition tested.

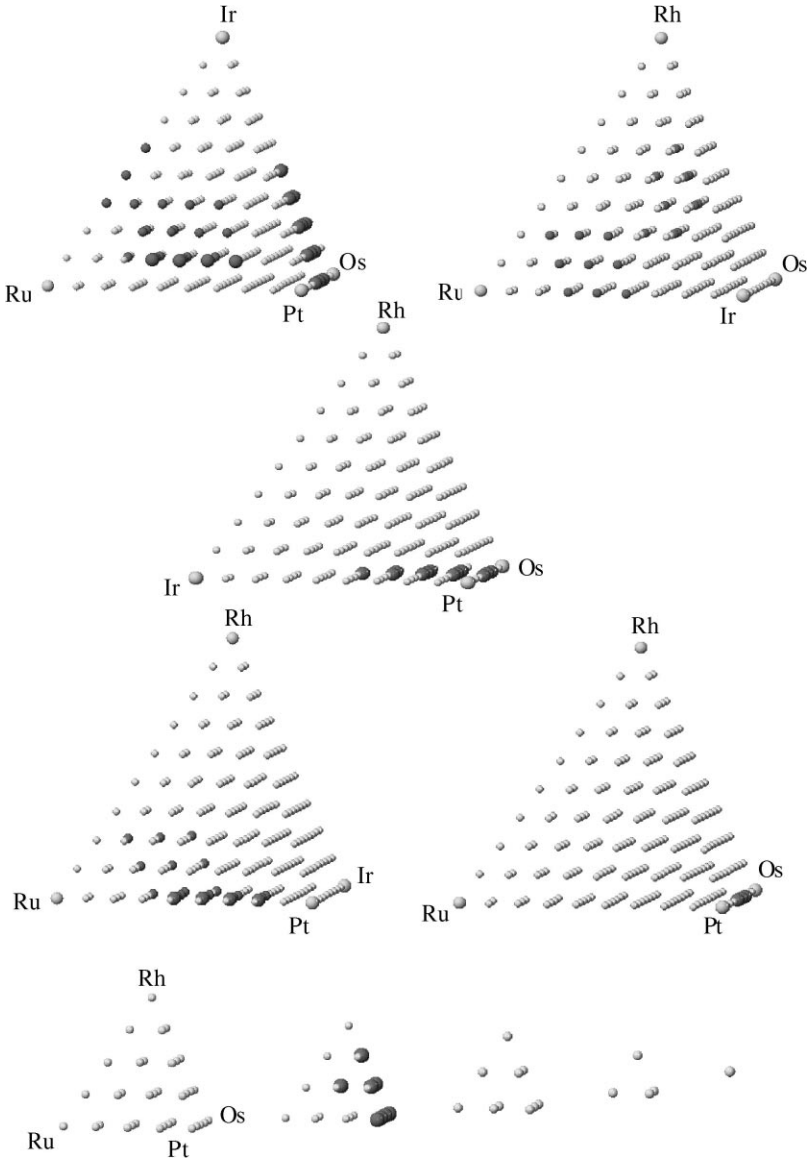

Fig. 2. Catalyst activity map for oxygen evolution. Large and small gray spheres indicate Ni–PTP fluorescence at +1350 and +1400 mV, respectively.

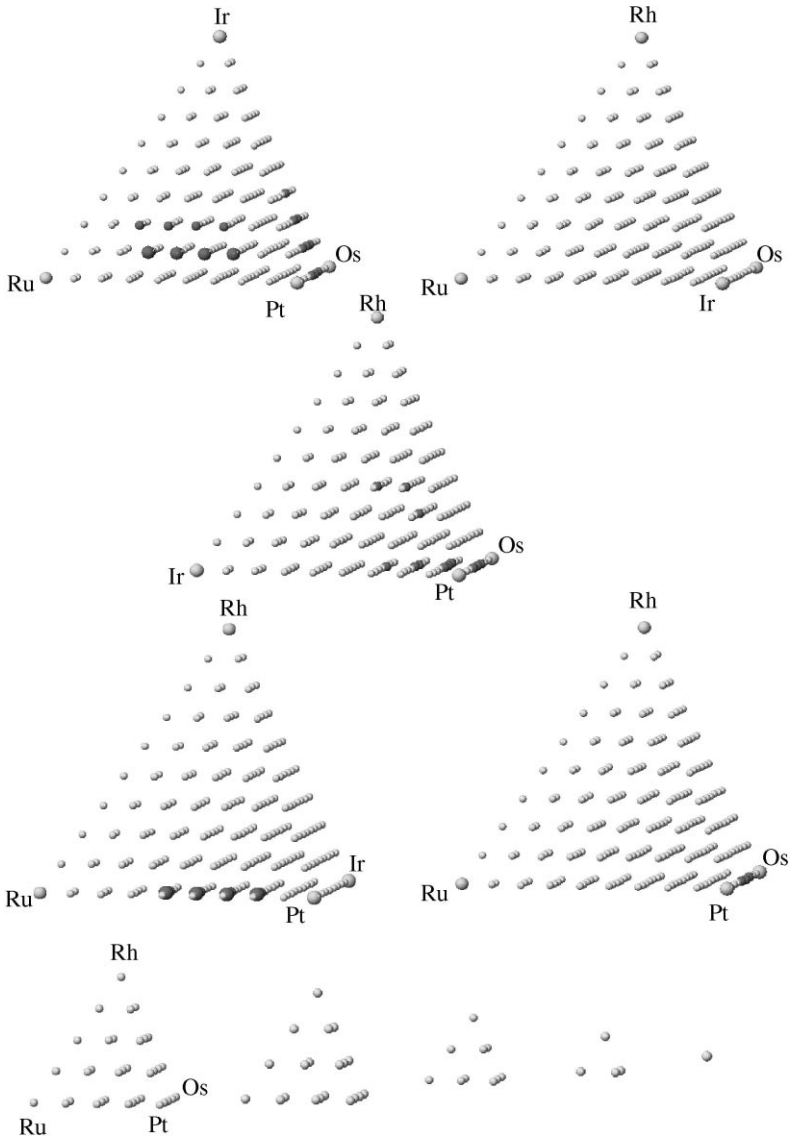

Fig. 3. Consensus map for bifunctional catalyst activity. Larger gray spheres indicate compositions that had the highest level of activity in Figs. 1 and 2. Note that the Pt–Ru–Ir ternary appears on the ternary faces of the two quaternary regions, so there is actually only one region of highest bifunctional activity. Smaller gray spheres indicate combinations of highest and next highest activity rankings from Figs. 1 and 2.

In the quaternary sections, the spheres at each vertex represent a composition that is 100% (99/99) in the element indicated. Along each binary edge, the compositions change in 11/99 increments of the element indicated at the distal vertex. The same geometrical pattern continues through the whole tetrahedron, with spheres located on each outer triangular surface (except those on the binary edges) representing ternaries and spheres located in the interior representing quaternaries. For pentanary compositions, five tetrahedral sections are used to represent catalysts containing progressively greater amounts (11–55%) of iridium. Only Fig. 2 (oxygen evolution activity) shows highly active catalysts among these pentanary compositions.

Fig. 1 shows active catalyst compositions for the oxygen reduction reaction (2), and Fig. 2 shows a similar map for the water oxidation reaction (1). Fig. 3 is the consensus map, showing compositions that were active in both reactions. Note that there is only one small region (in the Pt–Ru rich region of the Pt–Ru–Ir ternary, which appears on the faces of two tetrahedra in Fig. 3) that represents consensus of the sizable "hot" zones in Figs. 1 and 2. There are also several zones of moderate activity, which represent a "hot–warm" consensus of the two activity maps. The catalyst arrays were conditioned anodically in order to eliminate unstable compositions, and so many of the alloy compositions that have reasonable activity for reaction (2) were destroyed by anodic corrosion prior to screening.

These screening experiments were done at relatively low resolution in order to identify composition zones of high activity. Within the active zones, one can interpolate and also find highly active catalsyts. For example, interpolating between $Pt_{55}Ru_{44}Ir_0$ and $Pt_{44}Ru_{44}Ir_{11}$, one finds the very active and stable composition $Pt_{49.5}Ru_{44}Ir_{5.5}$.

3.4. Bulk formulation and characterization of active catalysts

Two catalysts from the high activity zone in the consensus map, $Pt_{4.5}Ru_4Ir_{0.5}$ and $Pt_4Ru_4Ir_1$, were prepared in bulk form by borohydride reduction of the appropriate metal salts. For comparison purposes, Pt, Pt_1Ru_1, and Pt_1Ir_1 catalysts were also prepared. Table 1 shows the BET and electrochemically active surface areas of the catalysts. With the exception of PtRu, the catalysts have roughly similar surface areas. Powder XRD patterns showed that the crystalline portion of each catalyst, as prepared, contained only a nanocrystalline face-centered cubic phase. From the line widths of the diffraction peaks [33], the primary particle sizes are on the order of 2–3 nm for the binary and ternary catalysts, and about 9 nm for Pt metal.

Table 1
BET and electrochemically active surface areas of catalysts

Catalyst composition	BET surface area (m^2/g)	Active surface area (m^2/g)
Pt	22.4	11.3
$Pt_{4.5}Ru_4Ir_{0.5}$	25.3	12.0
$Pt_4Ru_4Ir_1$	30.8	15.7
PtRu	14.1	8.7
PtIr	26.2	14.0

XPS spectra, summarized in Table 2, show that Pt on the surface of each catalyst is in the zero oxidation state, whereas Ru (by comparison with RuO_2 and RuO_3, which have binding energies of 280.6–281.0 and 282.3–282.7 eV, respectively) exists as oxidized species rather than in metallic form (279.8–280.2 eV). The Ir binding energies show a mixed oxidation state, with metallic Ir in the range 60.6–61.0 eV and Ir^{3+} in the range 62.6–63.0 eV. Interestingly, the surface appears to be enriched in Pt, relative to the bulk composition. These are the apparent oxidation states and surface distributions in the as-prepared form of the catalysts, which are likely to change with electrochemical oxidation and reduction [34,35]. Under anodic conditions the surface is probably highly oxidized.

Fig. 4 shows anodic (water oxidation) and cathodic (oxygen reduction) polarization curves of the five catalysts in the gas diffusion cell. $Pt_{4.5}Ru_4Ir_{0.5}$ and PtIr are close to each other in catalytic activity for oxygen evolution, but PtIr is poor for oxygen reduction; similarly, $Pt_{4.5}Ru_4Ir_{0.5}$ and Pt are close to each other for oxygen reduction, but Pt is poor for oxygen evolution. Only $Pt_{4.5}Ru_4Ir_{0.5}$ has the highest activity in both modes. Under the testing conditions, $Pt_{4.5}Ru_4Ir_{0.5}$ resists corrosion while catalyzing both oxygen evolution

Table 2
XPS data for representative catalysts

Catalyst	Apparent atomic percentages (binding energies, eV)			
	Pt_{4f}	O_{1s}	Ru_{3d}	Ir_{4f}
$Pt_{4.5}Ru_4Ir_{0.5}$	28.9 (71.6)	56.6 (531.0)	10.7 (280.3, 281.1, 282.5)	3.8 (62.2, 63.1)
$Pt_4Ru_4Ir_1$	29.2 (71.7)	55.8 (531.0)	7.7 (280.5, 281.6, 283.1)	7.3 (61.3, 62.3)
PtRu	40.6 (71.6)	47.6 (531.0)	11.7 (280.3, 281.4)	–

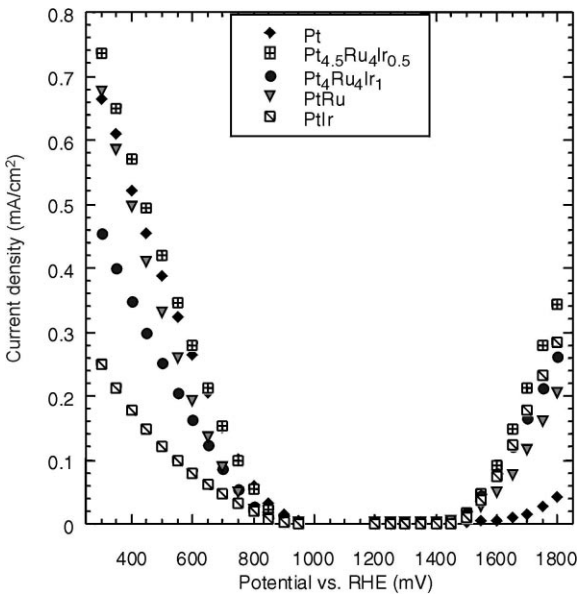

Fig. 4. Polarization curves of the oxygen electrode in electrolysis (oxygen evolution) and fuel cell (oxygen reduction) modes for the indicated catalysts.

and oxygen reduction at lower overpotentials than the other catalysts tested. PtIr also had good corrosion resistance. PtRu was unstable at high anodic potentials; a characteristic yellow-gold color was observed in the electrolyte solution after testing. UV–visible spectra showed absorbance peaks around 300 and 470 nm for electrolyte solutions from anodized PtRu. These peaks are attributed to RuO_4 (or H_2RuO_5) [36] from the dissolution of ruthenium. The difference in stabilities of PtRu and $Pt_{4.5}Ru_4Ir_{0.5}$ was also evident in SEM micrographs (Fig. 5). At 15,000× magnification, no obvious morphological differences were observed for $Pt_{4.5}Ru_4Ir_{0.5}$ before and after testing. PtRu, on the other hand, showed a much more porous texture after testing.

3.5. Mechanistic studies

To understand the difference in performance of the catalysts, a detailed mechanistic study was carried out. Because PtRu was unstable under the testing conditions, the kinetic studies were limited to a comparison of stable compositions $Pt_{4.5}Ru_4Ir_{0.5}$ and PtIr.

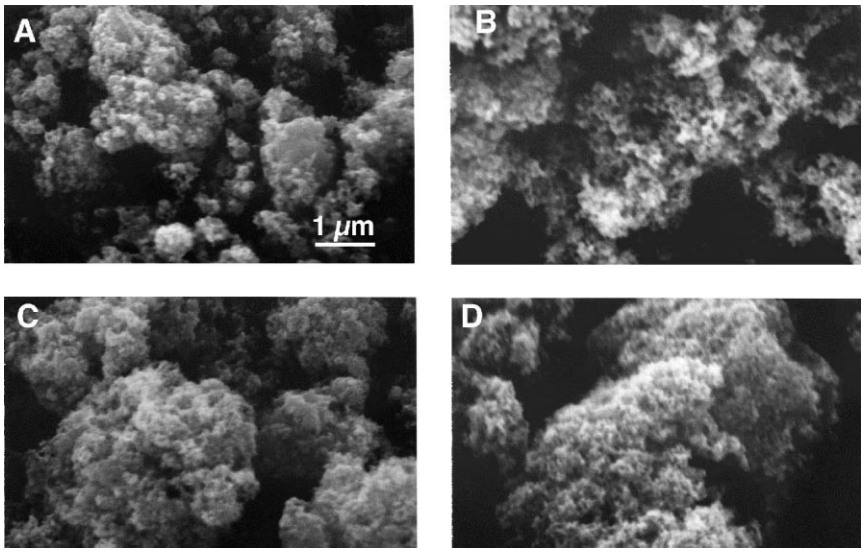

Fig. 5. SEM images of catalysts before and after electrochemical testing: (A) PtRu before; (B) PtRu after; (C) $Pt_{4.5}Ru_4Ir_{0.5}$ before; (D) $Pt_{4.5}Ru_4Ir_{0.5}$ after.

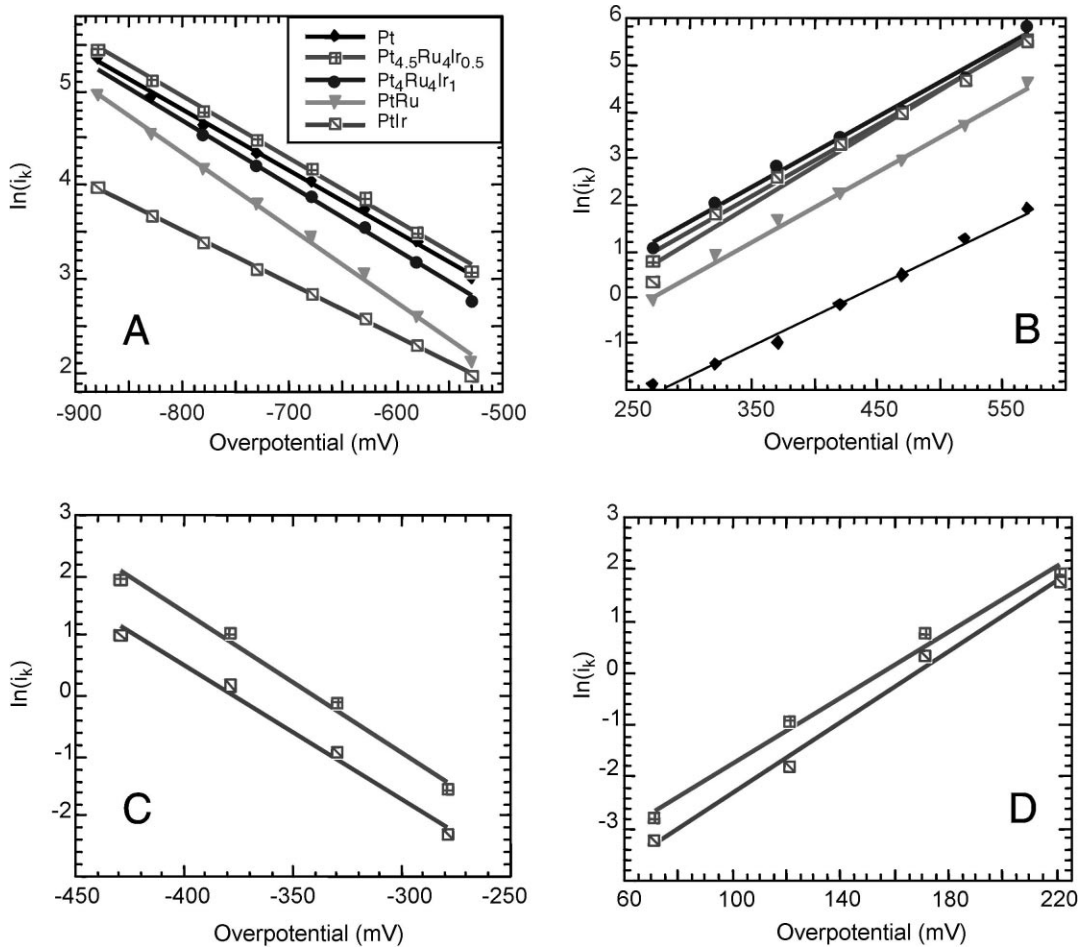

Fig. 6. Mass transfer corrected Tafel plots for: (A) oxygen reduction at high overpotential; (B) oxygen evolution at high overpotential; (C) oxygen reduction at low overpotential; (D) oxygen evolution at low overpotential.

Table 3
Kinetic parameters for oxygen evolution and oxygen reduction in 0.5 M H_2SO_4 at room temperature

Catalyst	Oxygen evolution			Oxygen reduction		
	Tafel slope (mV)		Apparent exchange current density (A/cm^2)	Tafel slope (mV)		Apparent exchange current density (A/cm^2)
	Low η	High η		Low η	High η	
$Pt_{4.5}Ru_4Ir_{0.5}$	30	66	3.6×10^{-7}	−43	−150	5.8×10^{-6}
PtIr	29	62	1.9×10^{-7}	−45	−180	2.7×10^{-6}

3.5.1. Tafel plots

The total current, i, is composed of the kinetic current i_k, and the mass transport limited current i_l, according to Eq. (3):

$$\frac{1}{i} = \frac{1}{i_k} + \frac{1}{i_l} \tag{3}$$

Further, at moderate to high overpotential, i is related to the exchange current, i_0, by Eq. (4):

$$i_k = i_0 \, e^{n\alpha F\eta} \tag{4}$$

in which η is the overpotential, n the number of electrons transferred, α the transfer coefficient and F, Faraday's constant.

Using a non-linear fitting program, the limiting current i_l was determined for each of the anodic and cathodic current–voltage plots shown in Fig. 4. Mass-transfer corrected Tafel plots ($\ln(i_k)$ vs. η) for the various electrocatalysts are presented in Fig. 6. For the anodic reaction, the Pt electrode showed a single Tafel slope, while all the remaining catalysts exhibited dual Tafel slopes. For the cathodic reactions, dual Tafel slopes were observed for all the catalysts. Tafel parameters at low and high overpotentials for the $Pt_{4.5}Ru_4Ir_{0.5}$ and PtIr catalysts are summarized in Table 3. For water oxidation, at high overpotentials, both catalysts show the same Tafel slopes (66 and 62 mV, corresponding to RT/F), whereas at low overpotentials, a smaller Tafel slope (30 and 29 mV, or $RT/2F$) was observed. The apparent exchange current densities, which were determined for each electrode by extrapolation of the mass-transfer corrected Tafel plots, reflect that $Pt_{4.5}Ru_4Ir_{0.5}$ is a significantly better catalyst for both water oxidation and oxygen reduction than PtIr.

3.5.2. pH dependence of current–potential data

In order to obtain more detailed mechanistic information about the electrode reactions, anodic polarization measurements were done as a function of pH in 0.5 M H_2SO_4/K_2SO_4 solutions. Anodic potentials at constant current are plotted as a function of pH for the $Pt_{4.5}Ru_4Ir_{0.5}$ catalyst in Fig. 7A and C. At high overpotentials, the potential has no pH dependence within experimental error. At low overpotentials, however, a slope of −0.030 V/pH (or $-RT/2F$) is found. Plots of current at constant potential vs. pH (Fig. 8A) gave a slope of 1, which means that the reaction order with respect to H^+ ions is −1. Consequently, the kinetic current for the evolution of oxygen at $Pt_{4.5}Ru_4Ir_{0.5}$ electrodes at low overpotentials can be formulated as in Eq. (5):

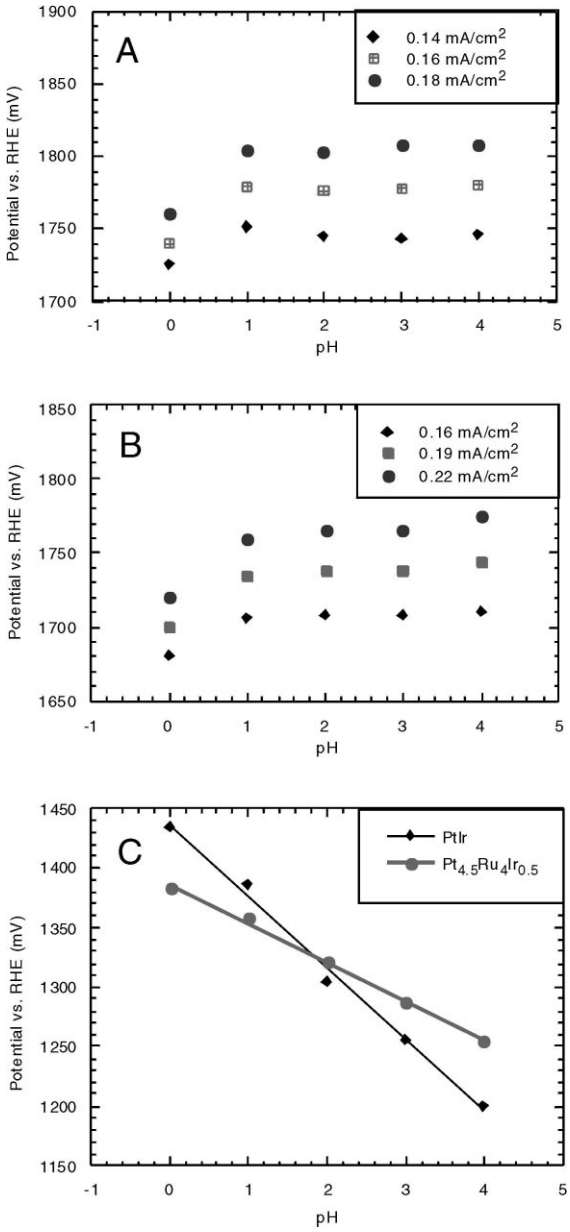

Fig. 7. pH dependence of electrode potential for: (A) $Pt_{4.5}Ru_4Ir_{0.5}$ at high current density; (B) PtIr at high current density; (C) $Pt_{4.5}Ru_4Ir_{0.5}$ and PtIr at low current density (2×10^{-3} mA/cm^2).

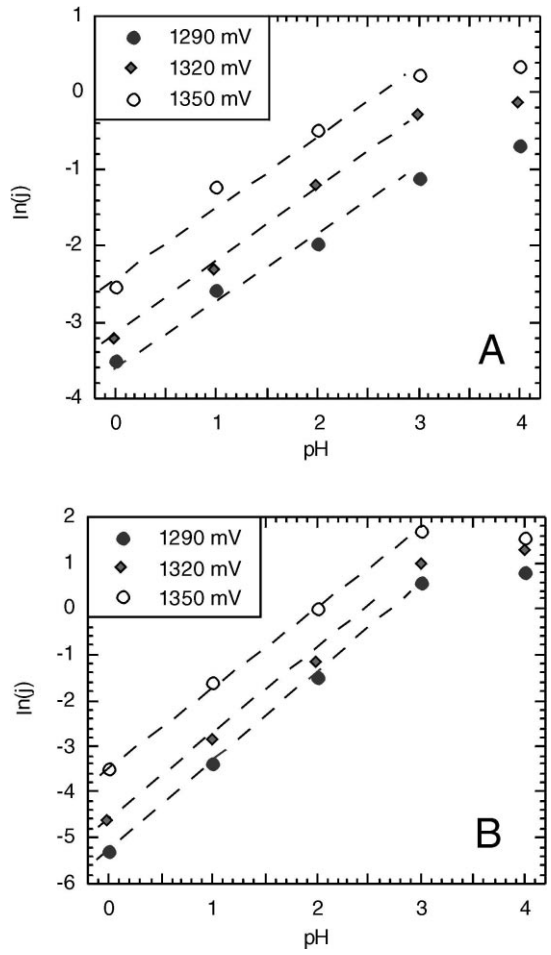

Fig. 8. pH dependence of the current density at various potentials for: (A) $Pt_{4.5}Ru_4Ir_{0.5}$; (B) PtIr.

$$i_k = nFAk(a_{H^+})^{-1} \exp\left(\frac{F\eta}{RT}\right) \quad (5)$$

where n, F, R, and T have their usual meanings, A is the electrode area, and k the rate constant of the reaction.

Anodic potentials for PtIr are plotted as a function of pH in Fig. 7B and C. At high overpotentials, changing the pH of the solution does not cause the potential to change, which is the same behavior as that observed for $Pt_{4.5}Ru_4Ir_{0.5}$. At low overpotentials, a slope of −0.060 V/pH (or $-RT/F$) was found for PtIr. A plot of current density at constant potential against pH (Fig. 8B) gave a slope of 2, corresponding to a reaction order of −2 with respect to H^+. Similarly, the kinetic current for evolution of oxygen at low overpotential at a PtIr electrode can be formulated as in Eq. (6):

$$i_k = nFAk(a_{H^+})^{-2} \exp\left(\frac{F\eta}{2RT}\right) \quad (6)$$

3.5.3. Evaluation of reaction mechanisms

The mechanism of the oxygen evolution electrode reaction was analyzed by Bockris and Damjanovic [37–39] and later in more detail by De Faria et al. [40]. The mechanism that was compatible with their observations is

$$S + H_2O \rightarrow S\text{–}OH + H^+ + e^- \quad (7)$$

$$S\text{–}OH \rightarrow S\text{–}O + H^+ + e^- \quad (8a)$$

$$S\text{–}OH + S\text{–}OH \rightarrow S\text{–}O + S\text{–}H_2O \quad (8b)$$

$$S\text{–}O + S\text{–}O \rightarrow 2S + O_2 \quad (9)$$

Here S represents a site at the electrode surface. Note that (8a) and (8b) provide alternative reaction pathways.

With the assumption that (7) is the rate-determining step, the current expressions and pH dependence can be derived as follows [38]:

$$i_k = nFAk \exp\left(\frac{\beta F\eta}{RT}\right), \quad \left(\frac{\partial V}{\partial \ln i}\right)_{pH} = \frac{RT}{\beta F} \quad \text{and}$$

$$\left(\frac{\partial V}{\partial pH}\right)_i = 0 \quad (10)$$

If (8a) is rate determining, then the following expressions result:

$$i_k = FAk(a_{H^+})^{-1} \exp\left(\frac{F\eta}{RT}\right), \quad \left(\frac{\partial V}{\partial \ln i}\right)_{pH} = \frac{RT}{2F}$$

$$\text{and} \quad \left(\frac{\partial V}{\partial pH}\right)_i = \frac{-RT}{2F} \quad (11)$$

and with (8b) as the rate-determining step, the following expressions result:

$$i_k = 2FAk(a_{H^+})^{-2} \exp\left(\frac{F\eta}{2RT}\right),$$

$$\left(\frac{\partial V}{\partial \ln i}\right)_{pH} = \frac{RT}{2F} \quad \text{and} \quad \left(\frac{\partial V}{\partial pH}\right)_i = -\frac{RT}{F} \quad (12)$$

By comparing these expressions with the experimental results, it is evident that for water oxidation, the

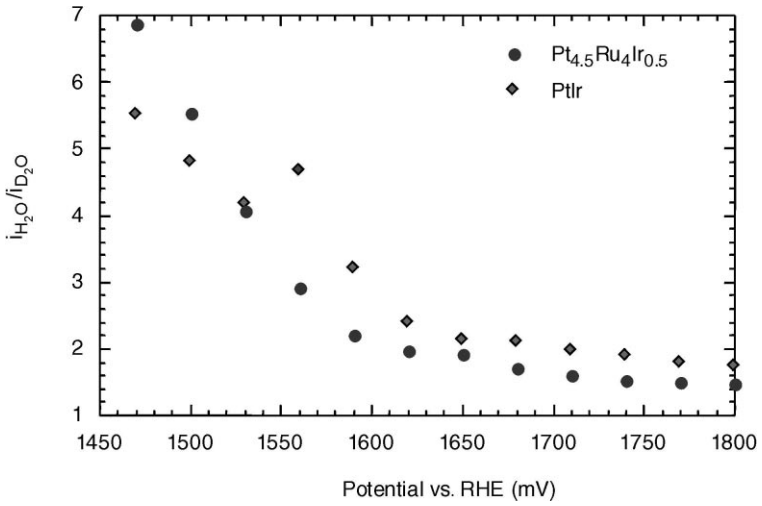

Fig. 9. Deuterium isotope effect on the water oxidation current at room temperature for $Pt_{4.5}Ru_4Ir_{0.5}$ and PtIr.

rate-determining step at high overpotentials is (7) for both the $Pt_{4.5}Ru_4Ir_{0.5}$ and PtIr catalysts. At low overpotentials, $Pt_{4.5}Ru_4Ir_{0.5}$ follows a reaction pathway with (8a) as the rate-determining step, whereas PtIr follows a pathway with (8b) as rate determining.

Since reaction (8a) and (8b) are alternative pathways in this mechanism, they occur in parallel [40]. A subtle point in this case is that for (8a) to be rate determining for a particular catalyst, it must occur *faster* than (8b) (but slower than (7)). Likewise, if (8b) is rate determining, it occurs faster than (8a). The addition of Ru to the PtIr catalyst increases the oxophilic character of the surface, increasing the strength of the S–O bond and therefore the acidity of S–OH groups. The result of this change is that step (8a) becomes faster than (8b) in the reaction catalyzed by $Pt_{4.5}Ru_4Ir_{0.5}$ at low overpotentials.

Smotkin and coworkers [41] have recently used deuterium isotope effects to study the mechanism of anode reactions in direct methanol fuel cells. A similar approach is possible in the present case, because steps (8a) and (8b) in the reaction mechanism involve transfer of protons. Fig. 9 shows the effect of substituting D_2O for H_2O in the anodic water oxidation reaction.

Table 4
Activation energy for oxygen evolution and oxygen reduction reactions on $Pt_{4.5}Ru_4Ir_{0.5}$ and PtIr catalysts in 0.5 M H_2SO_4

Potential E (mV vs. RHE)	$\Delta H(E)$ for oxygen evolution (kcal/mol)		$\Delta H(E)$ for oxygen reduction (kcal/mol)	
	$Pt_{4.5}Ru_4Ir_{0.5}$	PtIr	$Pt_{4.5}Ru_4Ir_{0.5}$	PtIr
550	–	–	3.58	4.87
580	–	–	3.68	5.08
610	–	–	3.84	5.16
640	–	–	3.99	5.86
1290	20.1	25.6	–	–
1320	19.6	22.7	–	–
1350	15.4	19.6	–	–
1470	11.1	13.6	–	–
1500	9.9	12.4	–	–
1530	8.3	11.1	–	–
1560	7.3	9.4	–	–
1590	6.4	8.2	–	–

Comparable kinetic isotope effects were observed for $Pt_{4.5}Ru_4Ir_{0.5}$ and PtIr electrodes over the applied potential range. At low overpotentials, the isotope effect is large for both catalysts, consistent with the transfer of protons in the rate-determining step ((8a) or (8b)). At high overpotential, where (7) is rate determining, the isotope effect becomes much smaller. The change in isotope effect with potential is consistent with the change in rate-determining step at about +1500 mV inferred from the pH dependence of the potential and current shown in Figs. 7 and 8.

To date, there is no general agreement on the mechanism of the four-electron oxygen reduction reaction (2) [42]. Because there were only slight differences between the activity of the best cathode electrocatalyst and that of Pt, detailed mechanistic studies of the oxygen reduction reaction were not attempted.

3.5.4. Temperature dependence of the electrode kinetics

The anodic and cathodic polarization curves at $Pt_{4.5}Ru_4Ir_{0.5}$ and PtIr electrodes were measured at various temperatures, and the activation energies for both reactions were calculated at each potential from Eq. (13) [39]:

$$\Delta H(E) = -R\left[\frac{\partial \ln i}{(1/T)}\right]_E \tag{13}$$

The activation energies for the anode and cathode reactions are listed in Table 4. For both reactions, the activation energies obtained are comparable to those reported previously for similar systems [36,43]. The activation energies at both $Pt_{4.5}Ru_4Ir_{0.5}$ and PtIr electrodes decrease with increasing overpotential. In all cases, the activation energy is lower at the more active $Pt_{4.5}Ru_4Ir_{0.5}$ electrode than at PtIr.

4. Conclusions

We have shown that combinatorial discovery can be used to identify better dual use catalysts, by superimposing activity maps to create a consensus map. Because the combinatorial method provides activity data for the entire composition space, it is more straightforwardly adapted to this task other than systematic optimization methods. While in this example the two figures of merit were catalytic activity for different reactions, in principle the same method could be used to optimize the activity and selectivity, or activity and some other property or properties simultaneously.

The ternary catalyst $Pt_{4.5}Ru_4Ir_{0.5}$ is superior to the previously described PtIr binary catalyst for both the water oxidation and oxygen reduction reactions. The pH dependence of the electrode kinetics was particularly useful in determining that the difference arises from stabilization of surface oxide species, which accelerates the oxidative deprotonation of surface OH groups.

Acknowledgements

We thank the Army Research Office for support of this work under grant DAAH04-94-G-0055, subcontract SA151-298 from Illinois Institute of Technology. DAD thanks the NSF Solid State Chemistry Program for support of his summer research at Penn State. We thank Prof. Eugene Smotkin for helpful discussions about kinetic isotope effects, and for providing a copy of Ref. [42] prior to publication. We also thank Dr. Renxuan Liu for designing the gas diffusion cell used to test bulk catalysts, and Mr. Chad Waraksa for writing the computer program used to analyze current–voltage data. We thank Dr. Rosemary Walsh and the electron microscope facility for the Life Sciences in the Biotechnology Institute at Pennsylvania State University for the use of the scanning electron microscope, and Dr. Jeffrey Shallenberger of the Penn State Materials Characterization Laboratory for obtaining XPS spectra.

References

[1] J.J. Hanak, J. Mater. Res. 5 (1970) 964.
[2] B. Jandeleit, D.J. Schaefer, T.S. Powers, H.W. Turner, W.H. Weinberg, Angew. Chem. Int. Ed. Engl. 38 (1999) 2494–2532.
[3] C.L. Hill, R.D. Gall, J. Mol. Catal. A 114 (1996) 103–111.
[4] M.T. Reetz, M.H. Becker, K.M. Kühling, A. Holzwarth, Angew. Chem. Int. Ed. Engl. 37 (1998) 2647–2650.
[5] A.C. Cooper, L.H. McAlexander, D.-H. Lee, M.T. Torres, R.H. Crabtree, J. Am. Chem. Soc. 120 (1998) 9971–9972.
[6] C. Hinderling, P. Chen, Angew. Chem. 38 (1999) 2253–2256.
[7] F.C. Moates, M. Somani, J. Annamalai, J.T. Richardson, D. Luss, R.C. Willson, Ind. Eng. Chem. Res. 35 (1996) 4801–4803.

[8] S.M. Senkan, Nature 394 (1998) 350–352.
[9] S.J. Taylor, J.P. Morken, Science 280 (1998) 267–269.
[10] P. Cong, R.D. Doolen, Q. Fan, D.M. Giaquinta, S. Guan, E.W. McFarland, D.M. Poojary, K. Self, H.W. Turner, W.H. Weinberg, Angew. Chem. Int. Ed. Engl. 38 (1999) 484–488.
[11] H. Scheffé, J. R. Stat. Soc. B 20 (1958) 344.
[12] J.A. Cornell, Experiments with Mixtures, 2nd Edition, Wiley, New York, 1990.
[13] E.A. Dawson, P.A. Barnes, Appl. Catal. 90 (1992) 217.
[14] J.E. Baker, R. Burch, S.E. Golunski, Appl. Catal. 53 (1989) 279.
[15] A.A.G. Lima, M. Nele, E.L. Moreno, H.M.C. Andrade, Appl. Catal. A 171 (1998) 31–43.
[16] J.F. McElroy, L.B. Butler, Integrated modular propulsion and regenerative electro-energy storage system (IMPRESS) for small satellites, in: Proceedings of the 10th AIAA/USU Conference on Small Satellites, Logan, UT, September 16–19, 1996.
[17] R. Poetter, Investigation of Autonomous Photovoltaic Systems with Storage Systems, Vol. 376, Fortschritt-Berichte VDI, Reihe 6, Energietechnik.
[18] K. Havre, B. Gaudernarck, Design configurations for stand-alone photovoltaic hydrogen systems, in: Proceedings of the Second Nordic Symposium on Hydrogen and Fuel Cells for Energy Storage, Helsinki, December 19–20, 1995.
[19] M.A. Hoberecht, R.D. Green, in: Proceedings of the 32nd Intersociety Energy Conversion Engineering Conference, Honolulu, HI, July 27–August 1, 1997, pp. 224–227.
[20] P.A. Lehman, C.E. Chamberlin, G. Pauletto, M.A. Rocheleau, Int. J. Hydrogen Energy 22 (1997) 465–470.
[21] L.A. Torres, F.J. Rodriguez, P.J. Sebastian, Int. J. Hydrogen Energy 23 (11) (1998) 1005–1009.
[22] O. Ulleberg, S.O. Morner, Solar Energy 59 (1997) 271–279.
[23] E.W. Justi, E.A. Winsel, Kalte Verbrennung-fuel Cells, Franz Steiner Verlag, Wiesbaden, 1962, p. 248.
[24] L.L. Swette, J. Giner, J. Power Sources 22 (1988) 399–408.
[25] H.P. Dhar, J. Appl. Electrochem. 23 (1993) 32–37.
[26] Z. Shao, B. Yi, M. Han, J. Power Sources 79 (1999) 82–85.
[27] L.L. Swette, A.B. Laconti, S.A. McCatty, J. Power Sources 47 (1994) 343–351.
[28] E. Reddington, A. Sapienza, B. Gurau, R. Viswanathan, S. Sarangapani, E.S. Smotkin, T.E. Mallouk, Science 280 (1998) 1735.
[29] G. TamizhMani, J.P. Dodelet, D. Guay, L. Dignard-Bailey, J. Electroanal. Chem. 444 (1998) 121.
[30] B.R. Rauhe Jr., F.R. Mclarnon, E.J. Cairns, J. Electrochem. Soc. 142 (4) (1995) 1073.
[31] M.S. Wilson, S. Gottesfeld, J. Appl. Electrochem. 22 (1992) 1.
[32] E. Reddington, J.-S. Yu, A. Sapienza, B.C. Chan, B. Gurau, R. Viswanathan, R. Liu, E.S. Smotkin, S. Sarangapani, T.E. Mallouk, Combinatorial discovery and optimization of new electrocatalysts, in: H. Fenniri (Ed.), Combinatorial Chemistry: A Practical Approach, Oxford University Press, Oxford, in press.
[33] H.P. Klug, L.E. Alexander, X-ray Diffraction Procedures for Polycrystalline and Amorphous Materials, 2nd Edition, Wiley/Interscience, New York, 1974, pp. 656–657.
[34] P.L. Hagans, K.E. Swider, D.R. Rolison, Proc.-Electrochem. Soc. 97 (13) (1997) 86.
[35] J.W. Long, R.M. Stroud, K.E. Swider, D.R. Rolison, J. Phys. Chem. B 104 (2000) 737–744.
[36] C. Iwakura, K. Hirao, H. Tamura, Electrochim. Acta 22 (1977) 329.
[37] J.O'M. Bockris, J. Chem. Phys. 24 (1956) 817.
[38] A. Damjanovic, in: J.O'M. Bockris, B.E. Conway (Eds.), Modern Aspects of Electrochemistry, Vol. 5, Plenum Press, New York, 1969, p. 369.
[39] A. Damjanovic, A. Day, J.O'M. Bockris, Electrochim. Acta 11 (1966) 791.
[40] L.A. De Faria, J.F.C. Boodts, S. Trasatti, J. Appl. Electrochem. 26 (1996) 1195.
[41] H.-W. Lei, S. Suh, B. Gurau, R. Liu, B. Workie, E.S. Smotkin, J. Am. Chem. Soc., submitted for publication.
[42] M.R. Tarasevich, A. Sadkowski, E. Yeager, in: B.E. Conway, J.O'M. Bockris, E. Yeager, S.U.M. Khan, R.E. White (Eds.), Comprehensive Treatise of Electrochemistry, Vol. 7, Plenum Press, New York, 1983, p. 301.
[43] R. Adzic, in: J. Lipkowski, P.N. Ross (Eds.), Electrocatalysis, Wiley, New York, 1998, p. 197.